A deep CNN approach to decode motor preparation of upper limbs from time–frequency maps of EEG signals at source level

A deep CNN approach to decode motor preparation of upper limbs from time-frequency maps of EEG signals at source level

Nadia Mammone[a,*], Cosimo Ieracitano[a,**], Francesco C. Morabito[a]

[a] *DICEAM, University Mediterranea of Reggio Calabria*
Via dell'Università 25, 89124 Reggio Calabria (Italy)

Abstract

A system that can detect the intention to move and decode the planned movement could help all those subjects that can plan motion but are unable to implement it. In this paper, motor planning activity is investigated by using electroencephalographic (EEG) signals with the aim to decode motor preparation phases. A publicly available database of 61-channels EEG signals recorded from 15 healthy subjects during the execution of different movements (elbow flexion/extension, forearm pronation/supination, hand open/close) of the right upper limb was employed to generate a dataset of EEG epochs preceding resting and movements onset. A novel system is introduced for the classification of premovement vs resting and of premovement vs premovement epochs. For every epoch, the proposed system generates a time-frequency (TF) map of every source signal in the motor cortex, through beamforming and Continuous Wavelet Transform (CWT), then all the maps are embedded in a volume and used as input to a deep CNN. The proposed system succeeded in discriminating premovement from resting with an average accuracy of 90.3% (min 74.6%, max 100%), outperforming comparable methods in the literature, and in discriminating premovement vs premovement with an average accuracy of 62.47%. The achieved results encourage to investigate motor planning at source level in the time frequency domain through deep learning approaches.

Keywords: Brain Computer Interface, Electroencephalography, Deep Learning, Convolutional Neural Network, Time-Frequency Analysis, Beamforming.

*Corresponding author
**Co-first author
Email addresses: nadia.mammone@unirc.it (Nadia Mammone), cosimo.ieracitano@unirc.it (Cosimo Ieracitano), morabito@unirc.it (Francesco C. Morabito)

1. Introduction

Brain Computer Interface (BCI) is a research field that covers a wide variety of advanced methods aiming at detecting and decoding brain's intention and thoughts. Current non-invasive BCIs systems mainly rely on electroencephalographic (EEG) sensorimotor rhythms (SMR) associated with the imagination of movements [1]. However, SMR-based BCIs are still far from being natural because they can somehow reliably discriminate between sustained imagination of moving the right or left hand or feet [2] and, in order to overcome the ability to discriminate between a limited number of classes, more complex commands (for example hand open/close) are usually associated to the motor imagery (MI) of feet or of a rotating object [3]. This unnatural mechanism requires an intensive users training and causes a significant delay between the intention and the issued control command [1]. Such a delay undermines the positive effects that BCI rehabilitation systems may have on neural plasticity (plasticity can be stimulated, for example, by watching the desired movement displayed on the screen) and makes such an approach not applicable whenever the aim is to control a device in a natural way. On the contrary, being able to detect and decode the intention/attempt to make a movement could generate the desired command without delays due to the need of sustained motor imaging. Furthermore, plasticity stimulation would greatly benefit from the ability of the BCI system to decode the intention/attempt to perform different sub-movements of the same limb from EEGs, which is very challenging due to the inherent limitations of EEG technique (poor spatial resolution and noise) [4].

Decoding movement preparation is useful whenever the aim is to control a device or an avatar (like in a rehabilitation scenario). The BCI system is designed to decode the intention of movement and to provide a control or a visual feedback of the movement that the subject intends to perform. In case of patients where the movement is correctly planned but the ability of muscles to implement the desired movement is partially or totally lost (for example, in myopathies or dystrophies), the desired movement could be detected and displayed or used to control a device. In case of patients who could benefit from rehabilitation to compensate for motor deficits, watching an avatar fully reproducing the intended movement that the subject can only partially carry out, would stimulate the plasticity of the neural motor circuitry [5]. Inspired by this principle and by the pioneering work of Ofner et al. [6], we decided to investigate if motor preparation of different sub-movements of the same limb maps differently into the neural signals. Since each subject plans movements at a neural level in a unique way [7, 8, 9, 10], BCI systems usually include a calibration phase [3] in order to optimize their own ability to interpret the specific patterns of the single subject. This means that BCI systems should be as much as possible data-driven. Hence we propose a method based on Deep Learning (DL) to discriminate the subject-specific patterns of motion preparation from neurophysiological signals. EEG allows to record neural activity non-invasively [11] and is widespread, low-cost, fast to set up, very well tolerated by subjects, and even widely used to monitor neurological disorders [12], [13]. Nevertheless,

EEG is generally thought to be not able to provide sufficiently detailed information to reconstruct complex sub-movements, mainly because EEG records the mixed activity of large numbers of neurons due to volume conduction effects [11, 14, 15, 16].

In order to overcome this issue, in the present work, scalp EEG signals are firstly projected into the cortex (source space) by solving the inverse problem. Then, the motor cortex (premotor, supplementary motor (SMA) and primary motor areas) is selected for the analysis. In this way the effects of volume conduction can be mitigated and the spatial resolution improved [17]. Furthermore, since it has been shown that motor preparation comes with specific patterns both in the time and frequency domain [18], a Time-frequency (TF) approach is proposed. Indeed, TF analysis provides a view of how frequency characteristics of signals vary over time, which is of paramount importance in a dynamic process such as planning and control of movements [19]. Here, we hypothesize that movement intention can be decoded from the TF representation of the electrical activity in the motor cortex, in the time frame preceding the onset of motion. In particular, we hypothesized that a link exists between sub-movement planning and the mutual relationship between the time-frequency maps of spatial source locations in the motor cortex. Going more into details, we hypothesized that the convolution of time-frequency maps along the spatial source locations direction can provide information about motion planning. The proposed method takes into account the time-frequency behaviour of EEG sources at different spatial locations, thus it benefits from information derived from the combination of three domains: time, frequency and space. To this end, the TF maps of all source signals are stratified in a single 3D map (x: time, y: frequency, z: source) and used as input to a deep Convolutional Neural Network (CNN). Through convolutional layers, the developed DCNN could learn the intended movement from the mutual relationship between TF patterns of the various sources (i. e. of the various sub-areas of the motor cortex associated to that source locations), and discriminate if the brain is planning to trigger a movement and which movement is going to be performed. Specifically, in this study, the EEGs dataset provided by Ofner et al. [6] is taken into account, including six upper limb movement types (elbow flexion (EF), elbow extension (EE), forearm supination (SU), pronation (PR) and hand open (HO), hand close (HC)) and resting (RE) phases. The 1-versus-1 classification method is applied coming up with 21 classifiers that can be divided into two classification types (Table 2): premovement versus premovement (premov vs. premov) and premovement versus resting (premov vs. rest).

The main contributions of the present work can be summarized as follows:

- development of a method able to detect motion preparation by discriminating between EEG segments preceding the onset of motion and EEG resting segments;
- development of a DL system which is in principle able to discriminate between EEG segments preceding the onset of different kind of motion of the same limb (hand open/close, forearm supination/pronation, elbow

flexion/extension) via a DCNN classifier based on a 3D representation of TF maps;

- development of a EEG-BCI system potentially relevant in clinical real-world applications.

The rest of the paper is organized as follows: Section 2 summarizes the main contributions in the literature on deep learning approaches to motor intention and imagery. Section 3 describes the analyzed dataset and the proposed approach, including the proposed deep CNN based on the time-frequency mapping of the electrical activity in the motor cortex. Section 4 reports the results, whereas, Section 5 discusses the advantages and limitations of the present work while addressing future perspectives. Finally, Section 6 concludes the paper.

2. Related Work

To the best of our knowledge, DL has not been applied yet to the classification of signals acquired during motor preparation. Indeed, so far, DL has been applied to the standard EEG-based BCI systems: P300, steady state visually evoked potentials (SSVEP), motor imagery (MI) and passive BCI (for emotions and workload detection). EEG BCI are often based on features extracted from sensorimotor rhythms (SMR) recorded during motor imagery but other brain rhythms can also be exploited [20, 21]. However, SMR-based BCIs can reliably elicit only right vs left hand or feet movement imagination [3], although recent research suggests the possibility of more spatially specific detection [22, 6]. What makes MI a unnatural source of control of a BCI system is that the user is usually asked to generate a control signal by imaging a certain movement that often does not coincide with the desired movement (for example, imaging to move both feet in order to generate a hand-open command) because only right hand vs left hand vs feet movement can be somehow reliably discriminated from EEGs. Furthermore, it is often necessary to imagine the same movement for some seconds in order to achieve a good classification accuracy, which causes a delay that makes the human-machine interfacing process further less natural [1]. MI is very useful for communication purposes, for example in patients affected by locked-in syndromes [4], but less useful to translate a motor intention. To induce plasticity in neurorehabilitation applications, it was demonstrated that acceptable delays should be in the order of a few hundred milliseconds [18]. Since MI is the research domain in BCI closest to the field of detection of motor preparation, the major contributions of DL in MI are here summarized. In [23], a Deep Belief Network (DBN) was explored to classify motor imagery (right vs left hand) EEG recorded using three channels. The network outperformed filter bank common spatial patterns (FBCSP) and the BCI competition winner when using a specific network architecture. In [24], CNN and stacked autoencoders (SAE) were combined to classify EEG Motor Imagery signals (BCI competition IV, three EEG channels, right vs left hand). Temporal and frequency information were used as input to the proposed network and yielded a 9% improvement over the competition's winner. Sturm et

al. [25] applied Layer-wise relevance propagation (LRP) to deep learning for motor imagery classification to overcome one of the main limitations that come with DL: to give a neurophysiological interpretation of results. They classified EEG of right hand vs right foot motor imagery over 5 subjects and achieved the same accuracy of comparable non-deep methods but were able to formulate plausible neurophysiological insights about how DNN produced a decision. DNN was applied to BCI Competition IV dataset in a study of Schirrmeister et al. [26]. In particular, a 3-channels two-class EEG motor-imagery dataset, and a 64-electrode four-class the Mixed Imagery Dataset (MID), dataset were analyzed. Different DNN structures were trained and tested. They explored a shallow CNN, a deep CNN, a hybrid shallow + deep CNN and residual NN. Both the deep and shallow CNN significantly outperformed FBCSP, whereas the hybrid CNN and the residual NN did not. Kwon-Woo and Jin-Woo [27] applied capsule networks to discriminate between right vs left hand motor imagery on the BCI competition IV 2b dataset. Compared to the number of studies on EEG recorded during movement execution or movement imagery, only a few have attempted to classify the planned movement using only EEG data before movement execution. Lew et al. detected movement intention during self-paced reaching tasks by performing a two class classification movement initiation vs rest [28] with a sensitivity of 76%. Deng et al. attempt to classify a subjects intention to generate torque at the shoulder or elbow in four healthy subjects, achieving an average recognition rate of 76% [4]. Preliminary results from Hammon et al. [14] discussed the possibility to predict the reaching movement direction toward a target (left, center, right) using premovement EEG. Yang et al. [29] investigated the kinematics aspects of motor planning, in particular, characteristics in the alpha (0-4Hz) and beta (13-30Hz) range from the movement planning were correlated with the alpha and beta characteristics from the movement execution phase to predict speed and acceleration. Kim et al. [30] used premovement EEG to classify movement direction (right vs left, up vs down), achieving an accuracy ranging from 75% to 85%. In contrast to the aforementioned researches and motivated by the very good results that DL has been achieving in biomedical applications ([31], [32], [33]), here, we propose a DL based approach for the classification of EEG data recorded during motor preparation in order to discriminate between different complex sub-classes of movements of the same limb. To this end, the EEGs of 15 healthy subjects were processed. Specifically, the data come from the work of Ofner et al. [6] who shared high density EEG (61 channels) co-registered with glove sensor and exoskeleton data. To the best of our knowledge, this is the only first dataset comprising high-density EEG and movement data. Other available dataset provide only EEG data, eliciting information about the exact motion initiation and investigating motor preparation is therefore not possible. In their work, as regards motor execution, Ofner et al. [6] selected EEG epochs recorded during motion execution (hence after the onset of motion) and performed a "movement vs movement" and a "movement vs resting" comparison. They compared the 6 movement classes (elbow flexion/extension, forearm supination/pronation and hand open/close) against each other by training 15 binary classifiers according

to a one-to-one classification strategy. They also merged all movement classes into one and classified movement against rest class. In the present paper, since we are interested in motor preparation, we focused on epoch preceding the onset of motion and we performed two different classifications: 1) premovement vs rest (premov vs. rest): EEG segments (epochs) preceding motion onset are classified against EEG resting epochs, every movement class is compared to resting class separately in order to assess how accurately the intention to start one of the six movements (elbow flexion/extension, forearm supination/pronation and hand open/close) can be discriminated from resting state; 2) premovement vs premovement (premov vs. premov): EEG epochs preceding motion onset are classified against each other in order to assess how accurately the intention to start a specific movement can be discriminated from the intention to start any of the other movements.

3. Methodology

The flowchart of the proposed procedure is shown in Figure 1. In particular, Subsection 3.1 will describe the analyzed EEG database, Subsection 3.2 will describe how sources in the motor cortex were extracted by solving the inverse problem through beamforming, Subsection 3.3 will discuss how time-frequency analysis of sources is performed through CWT and Subsection 3.4 will introduce the proposed deep CNN architecture.

3.1. EEG data description

The dataset was made freely available by Ofner et al. and can be found at BNCI Horizon 2020 website ($http://bnci-horizon-2020.eu/database/data-sets$). The dataset is described in detail in [6]. To the best of our knowledge, this is the only publicly available BCI dataset including high density EEG (61 electrodes) recorded simultaneously with motion data (coming from a glove and an exoskeleton). 15 healthy subjects (age 22-40 years, mean 27$\pm$5 years) were enrolled and involved in the study. Nine subjects were female, all of them were right-handed except S01. All the information regarding the protocol approved by the Ethics Committee can be found in [6].

Subjects sat comfortably on a chair, in front of a computer screen, with an anti-gravity exoskeleton (Hocoma, Switzerland) supporting their right arm to avoid muscle fatigue. The subjects performed six types of movement of their right upper limb (elbow flexion/extension, forearm supination/pronation and hand open/close). EEG acquired during a resting state were recorded too. Subjects were instructed to perform cue-based sustained movements starting from a common neutral position (hand half open, lower arm extended to 120 degree and in a neutral rotation). At second 0, a beep sounded and a cross was displayed on the computer screen (subjects were instructed to fixate their gaze on the cross). Afterwards, at second 2, a cue was shown on the computer screen, indicating the required task (one of the six movements or rest). At the end of task execution, subjects moved back to the starting position. Every session consisted of 10 runs, each run including 6 movement classes and a rest class, thus

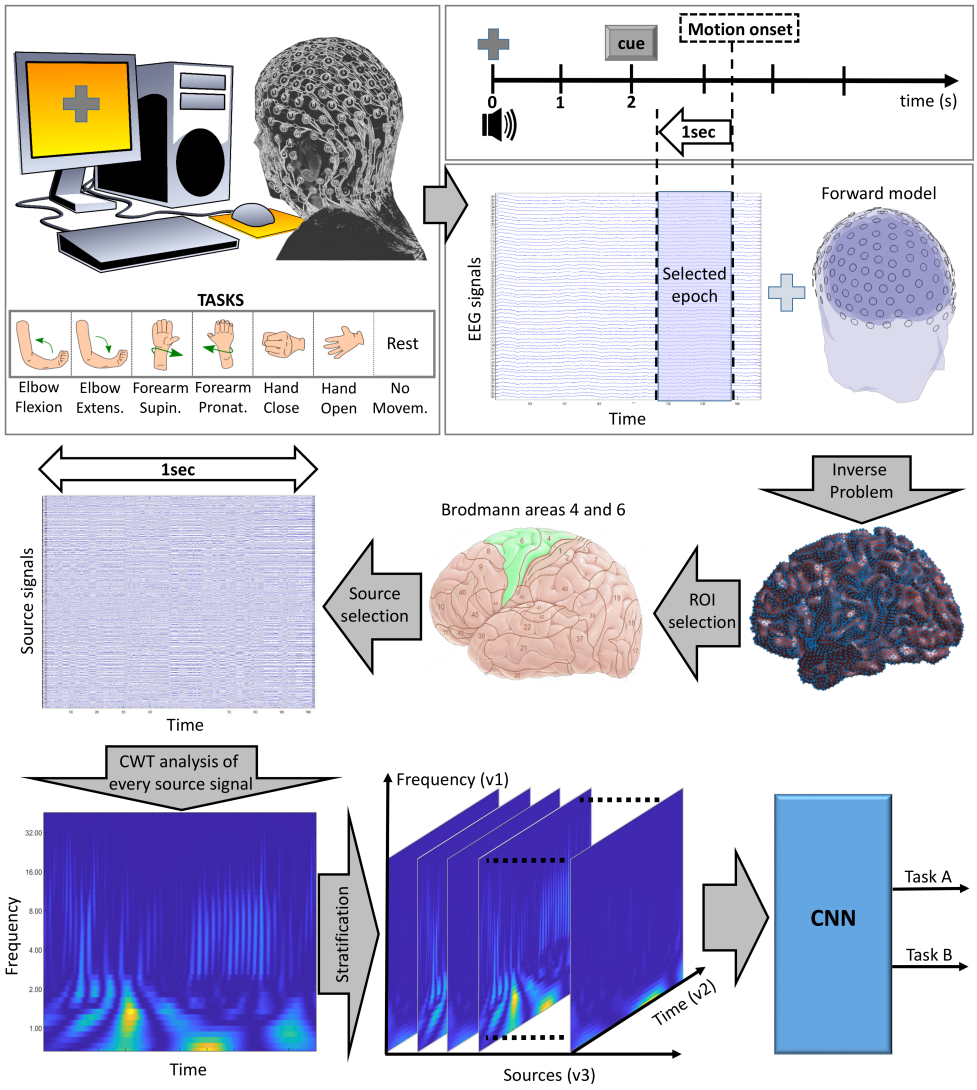

Figure 1: Flowchart of the proposed methodology. Up-left block shows the paradigm followed by Ofner et al. [6] for data collection (as regards the subplot showing tasks, permission has been obtained from the authors of [6]). The subject, based on a cue displayed on a screen, performs 6 different movements of the right upper limb or a resting task (no movement). The next block in the flowchart (up-right) shows how EEG epochs are selected starting from motion onset then moving one second backwards. Inverse problem is then solved on the selected epoch by taking into account the adopted forward model and source signals are estimated for every location of the head model. Source signals belonging to the region of interest (Brodmann areas 4 and 6) are then selected and passed through time-frequency (TF) analysis (Continuous Wavelet Transform). The TF maps of the sources are then stratified to build a volume (time x frequency x source) that is used to train a CNN to discriminate the task the subject is going to perform.

60 trials per class were recorded in a session. The EEG was collected through 61 channels uniformly distributed over frontal, central, parietal and temporal areas using active electrodes and four 16-channel amplifiers (g.tec medical engineering GmbH, Austria). Reference was placed on the right mastoid, ground on AFz. EEGs were bandpass filtered from 0.01 Hz to 200 Hz (8-th Chebyshev bandpass filter) and sampled with 512 Hz. Power line interference was suppressed with a notch filter at 50 Hz. Planning and implementation of a movement by the brain produces the so-called MRCP [18]. The MRCP includes three sub-potentials called readiness potential (RP) or Bereitschaft potential (BP), motor potential (MP), and movement-monitoring potential (MMP), which are thought to reflect movement planning/preparation, execution, and control of performance respectively [18]. BP starts to grow around 1.5 to 1 sec prior to the onset of movement. The width of the EEG segment preceding motion onset was set at 1 s in order to capture the window of motor planning. Therefore, for every subject 60 (= 10 runs x 6 trials) EEG segments (epochs) per movement class were available for the analysis and a comparable number of resting state EEG epochs were selected. In the end, 6300 (= 10 runs x 6 trials x 7 classes x 15 subjects) epochs were analyzed in the present study. Motion onset was determined as described in [6] from movement data coming from exoskeleton and glove. To ensure that motion onset detection was not biased by possible corruption of movement data, the estimated motion onset was visually checked for all of the 6300 epochs under examination.

3.2. Reconstruction of sources in the motor cortex from scalp EEG

A single active neuron produces intra-cellular and extra-cellular electromagnetic fields [11]. The fields generated by neighbouring neurons arranged in parallel sum up produce potential differences that may be collected on the scalp (electroencephalographic potentials). EEG thus reflects the electrical behaviour of the brain, which is of course related to the biochemical reactions associated with the inter-neuron communication that produces ongoing brains cognitive or motor tasks. To elicit information about current brain activity, such as motor planning, we can therefore study the brains electrical activity. In particular, as described in the Introduction, the motor cortex is believed to be in charge of planning and controlling movements [34, 35].

The EEG electrodes that cover the motor cortex are mainly the central ones (Figure 1), however, due to volume conduction effects, the field generated by a source overlaps to those generated by other neuronal sources during propagation through brain tissues. A single EEG electrode hence collects also the effects of sources not belonging to the underlying zone. As the aim of the present paper was to investigate motor planning of complex sub-movement (which we expect to involve the sub-areas in the motor cortex in a different way) we decided to study the problem at source level in order to reduce volume conduction effects and improve EEG spatial resolution. Source reconstruction involves a forward step and a inverse problem solution step which will be here shortly recalled.

3.2.1. Forward model and inverse problem solution

It is well established that neural activity can be modelled by intra- and extra-cellular current flows and that the electromagnetic behaviour of neurons responsible for EEG potentials collectable at scalp can be modelled by current dipoles [11]. Source reconstruction consists first of all in solving the so-called "forward problem", that consists in estimating the scalp potentials that would result from hypothetical current dipoles, or from a large number of dipoles, with the dipoles located according to a spatial grid that covers the entire brain volume or the cortical surface [36].

The so-called forward model of EEG data describes how the activity of neural sources in the brain projects into the sensors space (scalp). Such projection depends on the geometries and conductive properties of the different tissue which the neural fields propagate through (gray matter, white matter, cerebrospinal fluid, skull, skin) and must be embedded in the forward model. Considering the frequencies typically studied in EEG, the quasi-static approximation of Maxwells equations holds and the forward model can be assumed linear [37] and can be expressed according to the following equation:

$$\mathbf{x}(t) = \mathbf{G}\mathbf{q}_r(t) \tag{1}$$

where $\mathbf{q}_r$(t) is a 3 dimensional directed primary current vector (sized 3 x Ns, where Ns is the number of possible source locations in the cortex) associated to the location "r" (r=1,...,Ns); $\mathbf{G}$ is knows as "lead field" matrix (head model) and maps the primary currents $\mathbf{q}_r$(t) to the scalp potentials $\mathbf{x}$(t). It is sized Nc x $3Ns$, where Nc is the number of channels [37].

Solving the inverse problem consists in estimating $\mathbf{q}_r$(t)) given the collected signal $\mathbf{x}$(t) and a lead field matrix $\mathbf{G}$. In order to generate $\mathbf{G}$, a head model must be hypothesized.

The proposed methodology exploits the lead field matrix generated for the New York Head (NYH) by Haufe et al. [38], The locations of sources are known before-hand and the same head model is applied to every subject. NYH was selected in this work because it is a very detailed model of the head (six tissue types: scalp, skull, CSF, gray matter, white matter, air cavities) based on the the ICBM152 anatomy (a nonlinear average of the T1-weighted structural MRI of 152 adult subjects provided by the International Consortium for Brain Mapping). A finite element model (FEM) with a mesh of the cortical surface including 2000 nodes (i.e., source locations) was generated by [37] and is adopted in the present work. Source locations are shown in Figure 2. As regards the possible discrepancy between subjects, Haufe et al. [38] evaluated the possible discrepancies between the FEM model created from the individual anatomy and the FEM model created from the ICBM152 average head (AVG FEM) proposed by them. Their analysis was carried out over about 10000 locations covering the entire cortical surface. According to the relative MSE, the AVG FEM model outperformed all the other competing models [38].

Once the lead field matrix $\mathbf{G}$ has been estimated, given the real EEG data $\mathbf{x}$(t) measured at the scalp, solving the so-called "inverse problem" consists in

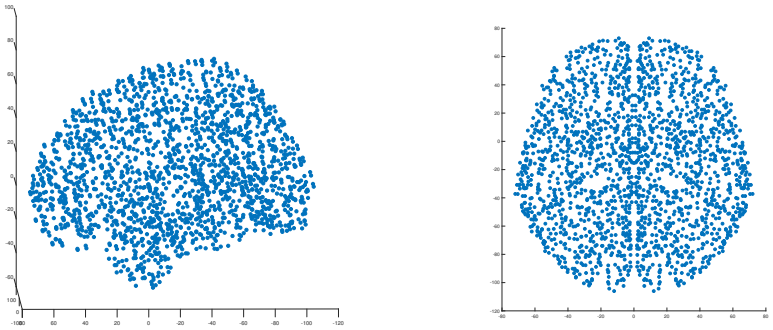

(a) (b)

Figure 2: Sagittal (a) and horizontal (b) view of the 2000 nodes of the 3D mesh of the cortical surface used in the present work [37].

estimating the sources $\mathbf{q}_r(\mathrm{t})$ that generated $\mathbf{x}(\mathrm{t})$.

What makes inverse problem solution challenging is the need to estimate a number of dipoles that is much larger than the number of available sensors. In this paper, for example, 2000 current dipoles must be estimated from 61 EEG signals. The problem is therefore ill posed and an infinite solutions exist.

Many approaches to inverse problem solution can be found in the literature and the most popular approaches in EEG source imaging are: minimum-norm solutions, beamformers, and dipole modeling [36, 39].

Whenever sources are expected to be focal (in focal epilepsy or in case of sensory evoked responses) single dipole model can be the best choice. Whenever the activity under examination is expected to be spatially distributed, the minimum norm method allows to make the least restrictive a-priori hypothesis [40, 39]. Linearly constrained minimum variance (LCMV) beamformers represent a trade-off between dipole modelling and minimum norm. LCMV estimates the source activity at each source location through spatial filtering. The proposed method solves the inverse problem through LCMV beamforming approach as the activity related to motion preparation is expected to be localized in space but not focal [39]. Furthemore, the advantages of using beamforming in EEG data recorded in BCI applications have been proven by Grosse-Wentrup et al. [41]. LCMV will be here recalled shortly.

3.2.2. Beamforming to solve inverse problem

Beamformers have the advantage that the number of dipoles must not be assumed a-priori. Beamforming techniques, originally introduced in radar signal processing, estimate the contribution of a single location in the brain into a measuring range. Beamformers calculate a linear combination of time series measured at the different sensors, in this case the EEG sensors. The aim is to extract the components originating from a desired direction or location while suppressing contributions from other locations.

The EEG distribution on the scalp is given by Eq. 1, where vector $\mathbf{x}$(t) represents the Nc x 1 vector of EEG samples collected at time t. The output of a beamformer is:

$$\widehat{\mathbf{q}}_r(t) = \mathbf{W}^T \mathbf{x}(t) \tag{2}$$

which represents the estimated contribution at the location of interest r. where $\mathbf{W}^T$ is a Ns x Nc spatial filtering matrix, Ns is the number of locations of interest in the head model, $\mathbf{x}$(t) is the Nc x 1 sample vector of observed data at time t from the Nc available sensors. Given a location of interest r, the spatial filter $\mathbf{W}^T$ should satisfy the following constraints:

$\mathbf{W}^T(r_i) * G(r_i) = I$

$\mathbf{W}^T(r_i) * G(r_j) = 0$

for every i not equal to j, I and 0 are sized 3 x 3 and represent the identity and the null matrices, respectively. If i is the current location of interest, sources located at j not equal to i are considered interfering sources whose influence should be maximally suppressed.

It can be demonstrated that $\widehat{\mathbf{q}}_r$ is a good approximation of $\mathbf{q}_r$ if the variance of the filter output is minimized [41], var($\widehat{\mathbf{q}}_r$) is minimized if:

$$\mathbf{W}^T = [\mathbf{G}^T * \mathbf{C}_x^{-1} * \mathbf{G}]^{-1} * \mathbf{G}^T * \mathbf{C}_x^{-1} \tag{3}$$

In this work, spatial filters $\mathbf{W}^T$ were estimated through the algorithm implemented by Haufe et al. [37] in Matlab.

3.2.3. ROI reconstruction

A Brodmann area is a region of the cerebral cortex defined by its cytoarchitecture, or histological structure and cells' organization. Brodmann areas are named after the German anatomist Korbinian Brodmann [42], they have been debated and refined in detail for a century and it is still the gold-standard cytoarchitectural model of organization of the human cortex (Figure 1).

We are particularly interested in the premotor (Brodmann area 6), supplementary motor (Brodmann area 6) and primary motor areas (Brodmann area 4), which are responsible for planning and implementing movements [34, 35]. These two areas therefore constitute our Region of Interest (ROI) and are shown in Figure 1. Once the spatial filters $\mathbf{W}^T$ were determined as described in Section 3.2.2, and the contribution (source signal) at each location of interest (among the 2000 provided by the head model described in Section 3.2.1) were estimated, the next step was to identify the locations belonging to the ROI. For each location of interest "r", starting from its Montreal Neurological Institute (MNI) stereotaxic coordinates, the corresponding Brodmann area was determined. To this end, MNI coordinates of the locations of interest in the cortex were first converted into Talairach coordinates through the algorithm developed by Lancaster et al. [43]. Then, the *Talairach Daemon* (www.talairach.org) [44, 45], a software that converts Tailarach coordinates into Talairach Atlas labels, was used to determine the Brodmann areas associated with every location. Talairach Atlas and MNI coordinates are the gold standard for the systems developed to analyze brain

data, like, for example, NeuCube [46]. After conversion by *Talairach Daemon*, the assigned label consists of five information: hemisphere, lobe, gyrus, tissue type, and cell type (for example: Left Cerebrum, Temporal Lobe, Inferior Temporal Gyrus, Gray Matter, Brodmann area 20). Different search options were available: single point, nearest gray matter, and cube range. In the present paper, the nearest gray matter search was adopted which involves concentric cube searches with varying diameters. Consecutively larger cubes (ranging from +/- 1mm (3mm wide) to +/- 5mm (11mm wide)) centered on the given coordinate are explored until a gray matter label is found.

Among all the 2000 possible locations of interest in the head model, it was therefore possible to select the 210 locations belonging to Brodmann areas 4 and 6. Each source signal belonging to the ROI was then analyzed in the TF domain through Continuous Wavelet Transform (CWT) [47] in order to study how its frequency content changed over the time.

3.3. Time frequency representation of cortical source signals

Each source signal was projected in the TF domain by the CWT [47]. Let s(t) be the single source signal in motor cortex extracted as explained in Sections 3.2.2 and 3.2.3:

$$CWT(a,b) = \frac{1}{\sqrt{a}} \int s(t)\psi^*(\frac{t-b}{a}) \tag{4}$$

where ψ represents the *wavelet mother* function, which is a template basis function of finite duration, zero mean and variable frequency content, a and b denote the dilatation (or scale) and shifting (or translation) variables (which determine how much the mother wavelet is scaled and shifted), $CWT(a,b)$ represents the wavelet coefficients and * the complex conjugate operator [47]. There is a one-to-one correspondence between scale and frequency, given the sampling rate and the chosen wavelet family (here, the *Daubechies 4* wavelet function was selected [47]). An approximate relationship between scale and frequency indeed exists where low scale values refer to high frequencies and viceversa ($f_a = \frac{f_c}{T_s a}$, with f_c central frequency of mother wavelet, T_s sampling period, f_a *pseudo-frequency* corresponding to the scale a). The trend of the scale-to-frequency relationship depends on the mother wavelet and the trend impacts on the resolution.

In this paper, the adopted wavelet mother was *db4* as it allowed to cover the desired range under analysis (0.6-45Hz) with a good resolution. This range covers the 5 main brain waves of general interest (delta, theta, alpha, beta and gamma) including MRCP, SMR, which are relevant to movement analysis [18]. Movement related artifacts in EEG (for example artifacts generated by chewing, electrode motion, head and limbs movements, etc) are one of the most challenging non-physiological source of noise that might corrupt EEG signals and therefore undermine the performance of EEG-based BCI decoders [48]. Filtering between 0.6Hz and 45Hz allowed us to save the information embedded in motor related cortical potentials, which lie in the low frequency range (<5Hz) [49], in sensory motor rhythms (nearly 12.5-15.5 Hz) and in beta band (nearly

13-30 Hz), while mitigating the effects of muscular artifacts (20-300 Hz) [50]. Given the sampling rate (512Hz) and the chosen wavelet family *db4*, a vector of 43 frequencies lying in the range (0.6-45Hz) was determined. In this way, for every epoch and for every source location r, a CWT matrix was computed. The spectrogram, which represents the percentage of energy for each wavelet coefficient, was then determined and it represents the TF map of source location r for the epoch under analysis. Explanatory spectrograms of a randomly selected source in the motor cortex in the 1-sec temporal window preceding motion onset are shown in Figure 3 for every task (premov or rest). Except the resting task, a change in the range 3-12 Hz is detectable 0.3 s before motion onset.

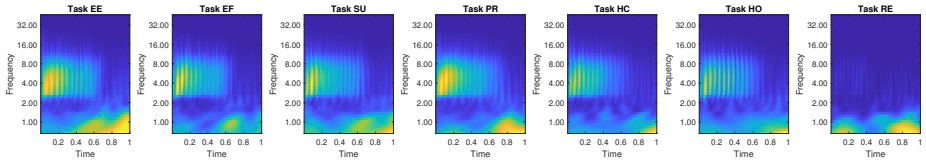

Figure 3: Explanatory spectrograms of a randomly selected source in the motor cortex of subject S01. Every subplot depicts the mean spectrogram of the corresponding task (Elbow Extension (EE), Elbow Flexion (EF), Forearm Supination (SU), Forearm Pronation (PR), Hand Close (HC), Hand Open (HO), Resting (RE)), averaged over the 60 trial available for that task. X-axis represents time whereas y-axis represents frequency. The time range is 1-second EEG preceding motion onset, motion starts at 1 s.

3.4. Deep Learning based Classification System

Deep CNN, as compared to standard machine learning classifiers, could help to fully automatize the complex classification of sub-movements discrimination. The use of deep learning schemes, that have shown great promise in aiding the interpretation of EEG signals on account of their ability to learn feature representations from raw data, may be of particular help in motor preparation decoding. Since the mechanism of motor preparation produces peculiar characteristics in EEG signals both in the time and frequency domains, the proposed method represents the time-frequency patterns of motor preparation through time-frequency maps. In this way, TF patterns in the signals reflect upon spatial patterns in the TF image, for example, Figure 3 shows that TF images reflect motor preparation: an energy reduction is indeed visible in the range 2-12Hz 0.3-0.4 s before motion onset and an energy increase in the range <2Hz (associated to the motor related cortical potential) starts being visible 0.5 s before motion onset. CNN are particularly powerful in extracting spatial features from images, furthermore, since we think that a key aspect in motor preparation is the spatial relationship between TF maps of different source locations in the motor cortex, we hypothesized that a CNN approach that convolves TF images with respect to sources (i. e. space), might help in discriminating motor preparation. As explained in the Introduction, in order to investigate how planning a desired movement correlates with EEG at source level, TF maps of cortical sources were used train a deep learning based classification system. TF maps of

the different 210 sources were not averaged but stratified in a 3D matrix so that the classifier could extract relevant information by combining the TF patterns of activation of different sources at cortical level to elicit the planned movement. Here, we propose a Customized Deep Convolutional Neural Network (DCNN). Theoretical concepts of CNN and details of the developed DCNN are reported as follows.

3.4.1. Convolutional Neural Network

Convolutional Neural Network (CNN) is a very common deep learning architecture typically used in images classification capable of achieving impressive results [51]. A CNN consists of a features extraction stage followed by a standard feedforward neural network (NN) employed to perform the discrimination task. The extractor processor includes N modules of *convolutional*, *activation* and *pooling* layers.

In the first layer, the dot product between a small sub-region of the input data and a bank of K filters (composed of multiple kernels stacked together) is computed. Each kernel sweeps over the input representation with stride s and sharing the same weights. The resulting output is a set of K feature maps. Specifically, let Z_j^l be the j^{th} feature map of the layer l and let Z_i^{l-1} be the i^{th} feature map of the layer $l-1$. The convolution is evaluated according to:

$$Z_j^l = \sigma(\sum Z_i^{l-1} * W_{j,i}^l + B_j^l) \tag{5}$$

where B_j^l represents the j^{th} bias of the layer l, $W_{j,i}^l$ is the weight matrix that connects features maps of adjacent layers (i.e., Z_i^{l-1}, Z_j^l), * denotes the convolution operator and $\sigma(\cdot)$ the non-linear activation function. The result is a feature map Z_j^l sized z_1^l x z_2^l, with:

$$z_1^l = \frac{z_1^{l-1} - k_1^l + 2p^l}{s^l} + 1 \tag{6}$$

and

$$z_2^l = \frac{z_2^{l-1} - k_2^l + 2p^l}{s^l} + 1 \tag{7}$$

where k_1^l, k_2^l are the kernel size at the layer l; z_1^{l-1}, z_2^{l-1} are the feature map size (or input data) at the the layer $l-1$; s^l (stride parameter) is the kernel step size used to slide over the input matrix and p^l is the zero padding parameter at the layer l.

In the second layer, a nonlinear activation function is applied to each feature map to learn nonlinear properties. Here, the well-known *Rectified Linear Unit* (ReLu, $f(Z_j^l) = max(0, Z_j^l)$) activation function is employed as it allows faster and more effective training [52].

The third layer, reduces the resolution of the input feature map by applying max or average pooling function. In this study, max pooling operator was

applied as it captures better invariant features and improves generalization performance. Specifically, the j^{th} kernel of layer l sized $\tilde{k}_1^l$ x $\tilde{k}_2^l$ slides over the j^{th} feature map (sized z_1^l x z_2^l) with a stride $\tilde{s}^l$, yielding a downsampled version of Z_j^l sized $\tilde{z}_1^l$ x $\tilde{z}_2^l$, with:

$$\tilde{z}_1^l = \frac{z_1^l - \tilde{k_1^l}}{\tilde{s}^l} + 1 \tag{8}$$

and

$$\tilde{z}_2^l = \frac{z_2^l - \tilde{k_2^l}}{\tilde{s}^l} + 1 \tag{9}$$

It is to be noted that, in this study, the proposed CNN was developed to support multi-channel input (i.e., volumetric data) of size v_1 x v_2 x v_3. However, in order to perform the convolution operation defined in 5, the input volume is firstly split into separated slices along the third dimension and then each slice convolved with the j^{th} k_1^l x k_2^l kernel to generate the corresponding z_1^l x z_2^l feature map.

3.4.2. Proposed Deep Convolutional Neural Network

Figure 4 reports the architecture of the proposed deep convolutional neural network. It consists of 3 convolutional layer (c_i, with i=1,2,3), each followed by a ReLU and max pooling module (p_i, with i=1,2,3). The network ends with a standard multi-layer NN with a softmax output layer. It is worth mentioning that the CNN topology has been chosen after several experimental tests according to the *trial and error* approach. Different CNN configurations have been tested by using different number of convolutional + pooling layers, filters and hidden layers in the multi-layer NN. Specifically, it has been observed that increasing the number of filters causes an increased computational complexity and, consequently, an increased computational cost, leading to a reduction of performances. Hence, we decided to take into account a limited number of filters of small size. Furthermore, in order to find out an efficient CNN topology, the performances were evaluated by increasing the number of processing layers. In particular, it has been observed that the overall premov vs. premov and premov vs. rest performances increased by making the CNN deeper. Indeed, the best classification accuracies were achieved with the architecture shown in Figure 4, which consisted of three convolutional (+max pooling) layers followed by a 2-hidden layer neural network with a softmax output layer. The proposed DCNN is meant to accept as input a data volume composed of v_3 time-frequency (TF) maps sized v_1 x v_2, where v_1 is the number of frequencies values ranged 0.6-45 Hz, while v_2 is the number of samples in a 1 s EEG epoch (that corresponds to the temporal window preceding the movement onset). Here, v_1=43, v_2=512 and v_3=210. At this stage, the TF volume $\mathbf{V}_j$ (v_1 x v_2 x v_3) is the input to the first convolutional layer (c_1) that includes K^{c_1}=8 learnable filters sized $k_1^{c_1}$ x $k_2^{c_1}$ x $v_3^{c_1}$ (where $k_1^{c_1}$=$k_2^{c_1}$=3, $v_3^{c_1}$=v_3=210), kernel step size s^{c_1}=1 and padding

parameter p^{c_1}=1. This operation produces K^{c_1} feature maps sized 43 x 512 (according to eq. 6 and 7). After applying ReLU activation function, each feature map is the input to the first max pooling layer (p_1), consisted of $\tilde{k}_1^{p_1}$ x $\tilde{k}_2^{p_1}$ = 5 x 4 kernels and stride $\tilde{s}^{p_1}$=2. The resulting output volume of size $\tilde{z}_1^{p_1}$ x $\tilde{z}_2^{p_1}$ x K^{c_1} = 20 x 255 x 8 is the input to the second convolutional layer (c_2) that includes K^{c_2}=16 learnable filters sized $k_1^{c_2}$ x $k_2^{c_2}$ x $v_3^{c_2}$ (where $k_1^{c_2}$=$k_2^{c_2}$=3, $v_3^{c_2}$=K^{c_1}=8), stride s^{c_2}=1 and p^{c_2}=1. Similarly to the first layer and after applying ReLU function, the second max pooling layer (p_2, consisted of $\tilde{k}_1^{p_2}$ x $\tilde{k}_2^{p_2}$ = 6 x 5 filters and stride $\tilde{s}^{p_2}$=2) outputs a feature maps volume $\tilde{z}_1^{c_2}$ x $\tilde{z}_2^{c_2}$ x K^{c_2} = 8 x 126 x 16. The last convolutional layer (c_3) includes K^{c_3}=32 learnable filters sized $k_1^{c_3}$ x $k_2^{c_3}$ x $v_3^{c_3}$ (where $k_1^{c_3}$=$k_2^{c_3}$=3, $v_3^{c_3}$=K^{c_2}=16), stride s^{c_3}=1 and p^{c_3}=1. The achieved feature maps are firstly processed by ReLU activation function and then by the last max pooling layer (p_3, filter size $\tilde{k}_1^{p_3}$ x $\tilde{k}_2^{p_3}$ = 6 x 6 and stride $\tilde{s}^{p_3}$=2), coming up with a feature maps volume of size $\tilde{z}_1^{p_3}$ x $\tilde{z}_2^{p_3}$ x K^{c_3} = 2 x 61 x 32. Finally, the features extracted from the last layer are reshaped and used as input to a conventional 2-hidden layers feedforward NN with 1000 and 500 units respectively. The DCNN ends with a softmax output layer to perform the 2-way classification tasks.

Table 1 reports the configuration set up and the total number of learnable coefficients of the proposed DCNN. For example, the number of parameters in the first convolutional layer c_1 is: $[(k_1^{c_1}$ x $k_2^{c_1}$ x $v_3^{c_1})+B^{c_1}]$* K^{c_1} = [(3 x 3 x 210)+1]* 8 = 15128; whereas, the number of parameters in the second convolutional layer c_2 is: $[(k_1^{c_2}$ x $k_2^{c_2}$ x $v_3^{c_2})+B^{c_2}]$* K^{c_2} = [(3 x 3 x 8)+1]* 16 = 1168. Overall, as can be seen in Table 1, the DCNN included a grand total of 4.5 * 10^6 coefficients.

3.4.3. Learning configuration

The proposed DCNN was trained using the Adaptive Moment (ADAM) optimization algorithm [53] minimizing the cross-entropy loss function and using mini-batch size of 21. The training process was stopped when convergence of loss function was observed (that is after 100 iterations). The learning parameters have been set up according with the practical guidelines reported in [53], [54] and the *trial and error* approach. In particular, we iterated over a broad range of hyper-parameter choices such as $\beta_1 \in$ [0, 0.9], $\beta_2 \in$ [0.99, 0.999, 0.9999], and log10(α) $\in$ [5, 1]. Experimental results showed that the best performances were achieved by using the default ADAM parameters (in terms of β_1=0.9, β_2=0.999, ϵ=10^{-8}) and a learning rate of α=10^{-4} (where α is the learning rate; β_1 and β_2 are the exponential decay rates for the first and second moment estimates, respectively; ϵ is a small constant used to avoid any division by zero). The proposed DCNN was developed with MATLAB R2018a (The MathWorks, Inc., Natick, MA, USA) and trained on high performance multi-GPU (two GeForce RTX 2080 Ti) installed on an Intel(R) Core(TM) i7-8000K CPU processor with 64 GB RAM. The network was trained and tested on each subject individually. In particular, 70% of epochs were used for training and the remaining 30% were used for testing. Notably, the training time was about of 10 minutes per subject and consequently of 2,5 hours considering all 15 subjects and one classification

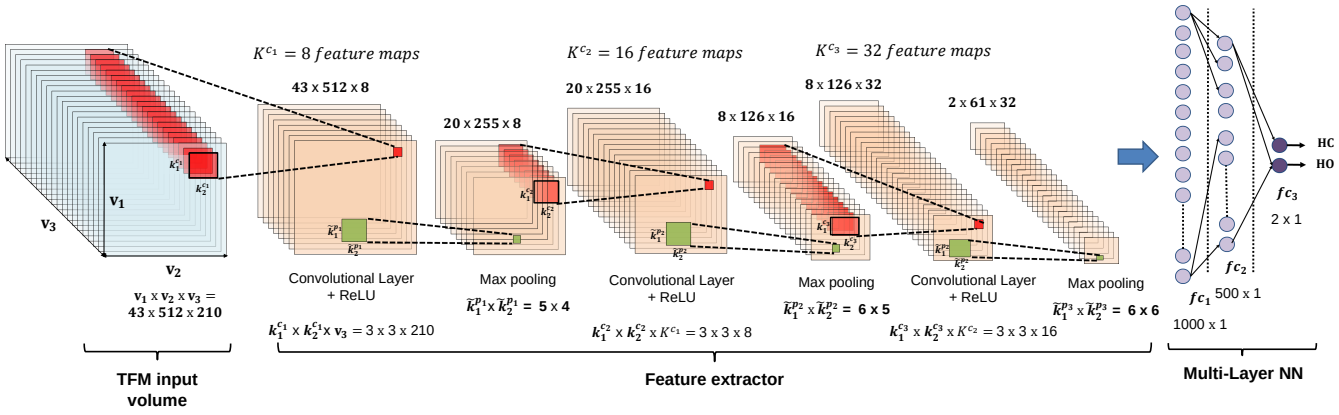

Figure 4: Architecture of the proposed Deep Convolutional Neural Network (DCNN). The Time-Frequency (TF) Maps input volume sized 43 x 512 x 210 is the input to the customized DCNN. It includes three convolutional layers followed by ReLu and max pooling operation (details are reported in Table 1). The network ends with a standard 2-hidden layers Neural Network (NN) for performing the binary classifications. As an example, in the figure, the DCNN performs the HC vs. HO classification task.

task (e.g. HC vs. HO).

Table 1: Details of the proposed DCNN and total number of learnable parameters.

Layer (l)	Layer Type	#Filters (K^l)	Filter Size	Stride (s^l)	Padding (p^l)	Feature Map	Weights	Bias	#Parameters
Input	Input Volume	-	-	-	-	43 x 512 x 210	-	-	-
c_1	Convolution	8	3 x 3 x 210	1	1	43 x 512 x 8	15120	8	15128
r_1	ReLU	-	-	-	-	43 x 512 x 8	-	-	-
r_1	max pooling	8	5 x 4	2	-	20 x 255 x 8	-	-	-
c_2	Convolution	16	3 x 3 x 8	1	1	20 x 255 x 8	1152	16	1168
r_2	ReLU	-	-	-	-	20 x 255 x 8	-	-	-
p_2	max pooling	16	6 x 5	2	-	8 x 126 x 16	-	-	-
c_3	Convolution	32	3 x 3 x 16	1	1	8 x 126 x 16	4608	32	4640
r_3	ReLU	-	-	-	-	8 x 126 x 16	-	-	-
p_3	max pooling	32	6 x 6	2	-	2 x 61 x 32	-	-	-
fc_1	Fully Connected	-	-	-	-	1000	3904000	1000	3905000
fc_2	Fully Connected	-	-	-	-	500	500000	500	500500
fc_3	Softmax	-	-	-	-	2	1000	2	1002
Total									**4427438**

4. Results

In this study, the database used in [6] and described in Section 3.1, was employed as benchmark to classify among six movement classes (HC, HO, PR, EE, EF, SU) and a resting (RE) class. To this end, a customized Deep Convolutional Neural Network was developed to perform two classification type: premov vs. premov and premov vs. rest (details are reported in Section 3.1). Notably, the 1 vs. 1 classification strategy was applied, yielding 21 binary classifiers as shown in Tables 2: 15 related to premov vs. premov and 6 related to premov vs. rest classification type, respectively. Each comparison (e.g. HC

vs. HO) included 120 epochs (60 per class) where 70% of data were used as training set and the remaining 30% the testing set. Conventional accuracy, precision, recall and F-score metrics were used to measure the classification performance [55]. Furthermore, the k-folds cross validation technique (with k=10) was employed to validate the classification. Hence, all results are reported as *average value* ± *standard deviation*. It is to be noted that, as F-score takes into account both precision and recall information, we refer only to F-score and accuracy parameters. Indeed, Table 2 and Table 3 report the accuracy and F-score values of the premov vs. premov and premov vs. rest classifiers. As regards premov vs. premov, the individual maximum classification accuracy of 98.41%±0.027 was achieved for subject S04 in the HO vs. EF discrimination task; whereas, the minimum accuracy performance of just 42.46%±0.073 was observed in subject S01 in HO vs. SU comparison. The average accuracies (and F-score) per subject (S01, S02,..., S15) and per discrimination task (HC vs. HO, HC vs. PR, etc...) were also evaluated. Specifically, the best premov vs. premov average individual accuracy and F-score were of 84.43%±0.051 and 84.64%±0.053, respectively (subject S04); while the highest discrimination task accuracy and F-score, were of 69.18%±0.062 and 68.42%±0.075, respectively (HC vs. SU). As regards premov vs. rest, the individual maximum classification accuracy was of 100% (subject S10, EE vs. RE comparison); whereas, the minimum accuracy performance was of 74.60%±0.103 (subject S07, PR vs. RE comparison). Also in this scenario, the averaged performance per subject and per discrimination task were estimated. Notably, higher classification results were observed: the best premov vs. rest average individual accuracy and F-score were of 97.49%±0.025 and 97.58±0.024, respectively (subject S10); while the highest discrimination task accuracy and F-score, averaged over all subjects, were of 91.33±0.057 and 89.57±0.067, respectively (PR vs. RE).

As expected, premov vs. rest was easier to classify than premov vs. premov cause during resting epochs the brain was planning no movement. It can also be noted that the performance was subjective, the subjects S03 and S04 are those that allowed to obtain the highest performances in premov vs. premov (up to 98%), for all subjects an average accuracy per task higher than chance level (50%) is obtained.

Figure 6 depicts the boxplots of the accuracies achieved in every paired premov vs. rest comparison over all the subjects. A given boxplot in Figure 6 includes the accuracies achieved over all the 15 subjects in comparison under analysis. Since a 10-fold cross-validation was adopted, for every premov vs. rest comparison 10 accuracies are estimated per subject, hence every boxplot accounts for 15 x 10 = 150 accuracy values. It is worth to note median accuracies lay significantly over 90% with a (p=3.7588e-10). The comparison between hand motor planning and resting achieved the highest accuracies, indeed the third quartile in HC vs RE and HO vs RE boxplots lay above 95%.

Similarly, Figure 7 shows the boxplots of the accuracies achieved in every premov vs. premov comparison. Median accuracies lay significantly (p=3.7446e-05) over the chance threshold (50%). The comparison between hand close and elbow and forearm motor planning achieved the highest accuracies, indeed the

third quartile in HC vs PR, SU, EE and EF boxplots lay above 75%.

In order to investigate the ability of the proposed system to decode TF maps of EEG and consequently extract relevant information for the classification of movement intention (from TF images of EEGs at source level), the features vector extracted by the deep CNN, sized 1000 x 1 (layer fc1 in Figure 4), was evaluated for both premov vs. premov and premov vs. rest classification type. It is worth noting that, to carry out this explanatory analysis, the subjects that reported the best and worst average discrimination performances in the premov vs. premov (as it represents the most difficult and challenging scenario) were taken into account (i.e., subjects S01 and S04, respectively). Specifically, as reported in Table 1, S01 shows an average accuracy of 52.55%, whereas S04 of 84.43%. The feature vectors related to the fc1 layer of the proposed deep CNN were evaluated for both the HC vs HO and the HC vs RE classification tasks (for both S01 and S04). Figure 5 shows the features' distribution of the pair of nodes that exhibited the largest distance between the centroids of the two classes (HC vs RE or HC vs HO). As can be seen, the extracted features showed very good separability properties in S01 (HC vs. RE, Figure 5 a) and S04 (HC vs. RE, HC vs. HO, Figure 5 b, d), ensuring high classification performance. As regards HC vs. HO classification task of S01, instead, overlapping features can be observed, which caused a misclassification of the HC/HO TF images under analysis (Figure 5 c).

5. Discussion

In the present paper, the challenging issue of decoding sub-movement intention of the same upper limb from EEG signals preceding motion onset was addressed. The importance of such topic is related to the possibility of implementing BCI-based rehabilitation systems or device controllers meant for all those subject who can in some extent plan movements but cannot or can only partially implement motor control. A BCI system able to detect and decode the planned movement from EEG signals could control an avatar on the computer screen or a device to make up for the subjects inability to implement motion. The present paper was inspired by the work of Ofner et al. [6], who collected and shared a dataset of high-density EEG (61 channels) and movement signals recorded during the execution of six different upper limb movements (elbow flexion/extension, forearm pronation/supination, hand open/close). Ofner et al. achieved an average accuracy in mov vs. rest of 87% and of mov vs. mov of 55%. The present paper is focused on the classification of motion preparation, therefore on the classification of EEG epochs preceding motion onset, which makes classification inherently more challenging because all the information related to motor initiation and control is missing. Nonetheless, the proposed system succeeded in discriminating premov from rest classes with an average accuracy of 90.3% which is higher than mov vs. rest accuracy achieved in [6] (87%) and higher than premov vs. rest performance achieved in [28] (sensitivity = 0.76±0.07%.). Motor preparation was discriminated from rest with high accuracy for every class of pre-movement, whereas the accuracy of premov vs.

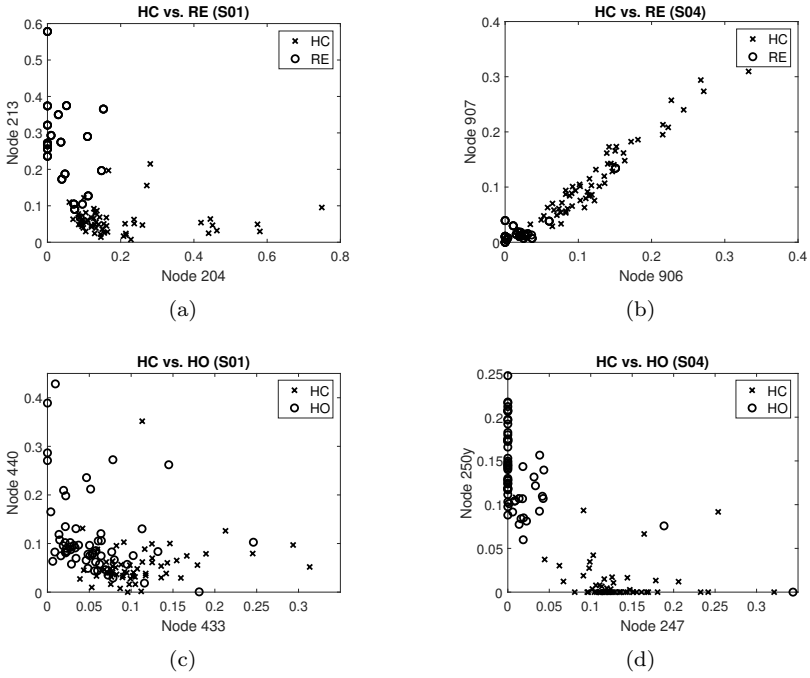

Figure 5: Scatter plot of the features extracted from the pair of nodes that maximized the distance between the centroids of the two classes (HC vs RE or HC vs HO). Every dot represents a trial among the 60 trials that the subjects executed for every task. The analysis was carried out on subject S01 (a-c) and S04 (b-d).

premov was lower (62.47%), as expected, since decoding complex movements from EEG is challenging. In particular, EEG-based BCI suffers from the low signal-to-noise ratio of EEG signals [15, 16] and from their nonstationarity over time, even EEG signals recorded from the same subject can vary between runs [3]. The achieved results suggest that information about the specific movement that the brain is going to perform is embedded in the EEG preceding motion onset. It was indeed possible to discriminate between premov and premov (elbow flexion/extension, forearm pronation/supination, hand open/close) with an accuracy above chance of (62.47%).

However, premov vs. premov accuracy is still low to be implemented in a practical BCI application, as unfortunately happens with BCI systems based on EEG which can still effectively discriminate only between right vs left motion execution/imagination [3]. The present work was able to reliably discriminate the intention to perform a movement from resting (premov vs. rest) and it encourages to pursue the implementation of EEG-based BCI for decoding submovements of upper limbs based on TF representations of the activity of cortical sources in the motor cortex, but some limitations exist.

First of all, the stage of inverse problem solution in the proposed methodology would benefit from dealing with high-density EEG with more than 61 channels [56], to this end, in the near future a 256-chans HD-EEG will be recorded, together with movement data, during the execution of various types of movement of the same upper limb. Increased spatial resolution at source level could aid the classifier in discriminating premov from premov. Another limitation of the present work is that the dataset is theoretically too small to train a CNN, nonetheless, motivated by the consideration that TF images are not deeply different from each other (see for example Figure 3), hence their layout is not variegated as it may happen in other common CNN applications of image classification, the performance of the proposed system was evaluated and it succeeded in distinguishing motor preparation phases from resting ones, which encouraged us to investigate the potential of DL in BCI applications despite the limited size of the dataset. Keeping in mind that DL will be able to fully show its own potential in BCI EEG signals classification only when very large dataset will be available, the authors have planned to collect EEG data at IRCCS Centro Neurolesi Bonino-Pulejo (Messina, Italy) from many subjects (nearly 100) in the near future. The dataset will include many trials per subject. The ability of DL to classify different premov task will be explored within subjects and across subjects.

Furthermore, given the limited size of the dataset, in the present study only binary classification was pursued, a multi-way classifier would have indeed required a very high number of training inputs. However, even the binary discrimination of sub-movements preparation of the same limb is of paramount importance. In fact, neurorehabilitation systems based on BCI are still in their infancy, they are currently based on the binary classification of right vs left motor imagery classification. Being able to discriminate between the preparation/imagery of even just two different submovements of the same upper limb would be a big step forward and would allow neuroscientists to develop more

effective and powerful BCI systems. This is the reason why the pairwise pre-submovement classification was considered a relevant goal in this work. When very large dataset will be available, DL will be able to disclose its own full potential and allow for reliably discriminating between two or more submovements preparation/imagery. How different submovements of the same limb are generated and controlled is still not clear, we think that the results reported in this paper encourage to apply DL to EEG signals at source level to shed a new light on motor preparation. In general, in order to be practically applicable, BCI systems should allow for a real time execution [9] which makes a pre-trained neural network an ideal candidate for the execution of very prompt classification. Another key aspect is calibration. BCI systems generally require a calibration phase that optimizes the performance of the system according to the specific features of the user's EEG signals [3]. However, re-training the network for each user would not be practically easy to implement as it would take a long time and would need high minimum hardware requirements. In the literature the importance of minimizing or avoiding the calibration steps is emphasized [3], which is even more important when dealing with neural classifiers. The collection of a wide cross-subject dataset will be pursued in the near future to train the network over multiple subjects ad investigate the possibility to avoid calibration. The present study could also be extended by evaluating the performance of the classification according to the selected cortical regions. Since many mechanisms of motor planning are still unexplored, other areas in the cortex may contribute to motor planning and thus to classification [34]. In this way, we could understand which areas contribute most to the classification of a given movements planning. In the future we will also try to classify motor preparation by performing the convolution not with respect to the source location (i. e. the sub-area in the motor cortex) but with respect to time and frequency. In this way, we could infer if time-frequency maps (convoluted with respect to the source), time-source (TS) maps (convoluted with respect to frequency) or frequency-source (FS) maps (convoluted with respect to time) contribute most to classification, in other words, we could infer if the intention of movement is more detectable in if TF, TS of FS patterns. Another possible extension of the present work would be hybrid signals processing. Hybrid BCI have not been widely explored so far, nonetheless, we think that EMG might bring a significant added value to motor intention decoding. EEG is useful to discriminate between left arm and right arm movements, however, it is difficult to classify different movements on the same arm. Tang et al. [57] introduced a two-step single-trial classification method to classify three movements (make a fist, hand extension and elbow flexion) of left and right arms by means of a hybrid EEG/EMG BCI. Tang et al. [58] also proposed a novel common spatial pattern (B-CSP) method based on Bhattacharyya distance to select the optimal frequency band of each EEG electrode. Signals in the optimal frequency band are decomposed into spatial patterns then the features that can describe the maximum differences of two classes of MI are extracted from EEG data. Vourvopoulos et al. [59] investigated both EEG-based and EMG-based BCI over four stroke patients, the achieved results suggested that patients with more se-

vere motor impairments may benefit from EEG-based neurofeedback, whereas patients with mild motor impairments may benefit more from EMG-based feedback. In the study of Zhang et al. [60], a novel multimodal human-machine interface system (mHMI) is developed using combinations of electrooculography (EOG), EEG and EMG to generate numerous control instructions. Six healthy subjects separately performed left and right hand motor imagery, looking-left and looking-right eye movements, and different hand gestures in different modes to control a soft robot in a variety of actions. Their results showed that the number of mHMI control instructions is significantly greater than with any of the individual modes. Tayeb et al. [61] introduces gumpy, a new free and open source Python toolbox developed for hybrid BCI. It is free, open source software and it provides different state-of-the-art techniques for processing and decoding EEG and EMG signals. In [62], the authors investigated the possibility of using EMG to detect rest vs intention to move the hand or wrist with the aim to perform robot-assisted training in individuals without residual movements. They compared two two-state (intention vs rest) detectors: an EEG-based movement intention detection (using only ipsilesional activity) and an EMG-based detector. Their study shows that severely affected stroke patients who have residual EMG, might trigger robot-assisted training via EMG signals, which require far less subjects training than EEG. For this reason, in the protocol of data collection that we planned to carry out at IRCCS Centro Neurolesi Bonino Pulejo, EMG signals will be also acquired along with high-density EEG.

6. Conclusions

In this work, the importance of decoding movement planning using EEG signals for Brain Computer Interface applications was discussed. Many subjects have a preserved ability to plan movements but a partial or total inability to implement them. Despite the importance of the topic, there are few works in the literature on motor planning and in general there are still few works on deep learning applied to EEG-based BCI. The objective of the present work is to develop and train an EEG-based classifier that automatically detects motor planning phases by discriminating them from resting phases (premov vs. rest). The second objective is to discriminate between motor planning of different movements of the same limb (premov vs. premov). To this end, a publicly available database of 15 subjects was analyzed which includes 61-channels EEG signals that were recorded during the execution of different movements of the same limb (elbow flexion/extension, forearm pronation/supination, hand open/close) and were co-registered with signals collected by motion sensors that allowed to determine the onset of the movement. A dataset of EEG epochs preceding the onset of movement and of resting epochs was constructed. A novel system based on a deep Convolutional Neural Network and the time-frequency representation of the electrical activity of sources in the motor cortex was introduced for the classification of such dataset. For every epoch, the system reconstructs source signals through beamforming and selects those belonging to the premotor and primary motor cortex; the system then constructs a time-frequency map of every

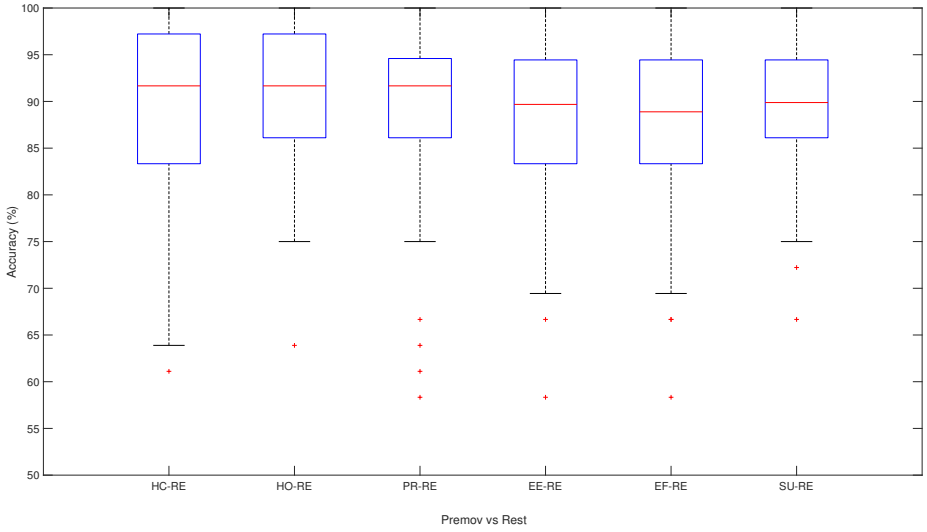

Figure 6: Boxplot of the accuracy achieved in premov vs. rest comparison. In the x-axis the different paired comparisons are represented. The horizontal line within each box represents the median, the edges of the box represent the first and third quartile, whiskers mark to the most extreme data points that are not considered outliers.

source through Continuous Wavelet Transform. A 3D matrix (time x frequency x source) is constructed with the TF maps of all the selected sources and a deep CNN is trained to recognize premov vs. resting or premov vs. premov classes. Analyzing the aforementioned dataset of 1-sec epochs preceding the onset of the movement, it was possible to discriminate motor planning from resting with an average accuracy of 90.30%, outperforming comparable methods in the literature, and to discriminate motor planning of different movements of the same limb with an average accuracy of 62.47%. Movement planning mechanisms are still largely unknown today and the present study suggests that studying the activation patterns of the premotor and motor cortex in the time-frequency-domain domain could help to describe them.

References

[1] G. R. Müller-Putz, A. Schwarz, J. Pereira, P. Ofner, From classic motor imagery to complex movement intention decoding: The noninvasive Graz-BCI approach, in: Progress in brain research, Vol. 228, Elsevier, 2016, pp. 39–70.

[2] J. Pereira, P. Ofner, A. Schwarz, A. I. Sburlea, G. R. Müller-Putz, EEG neural correlates of goal-directed movement intention, Neuroimage 149 (2017) 129–140.

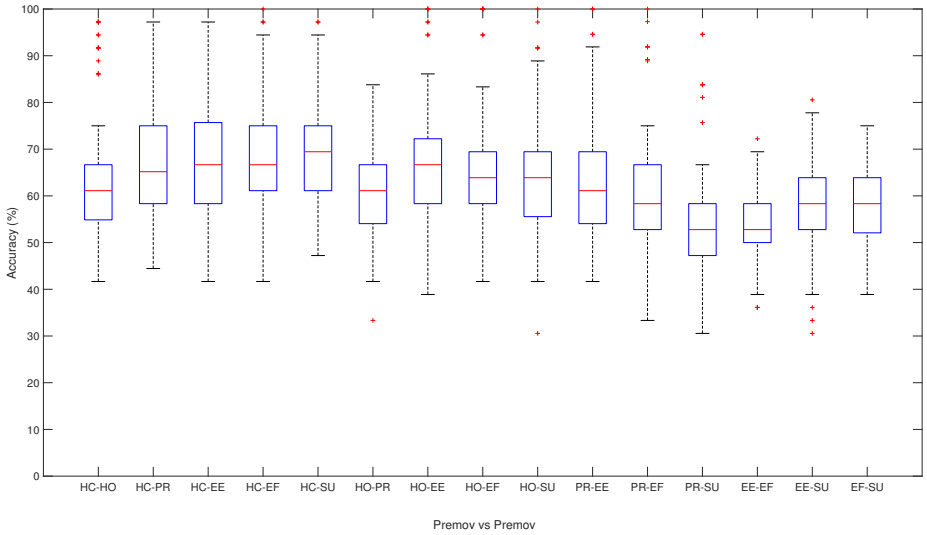

Figure 7: Boxplot of the accuracy achieved in premov vs. premov comparison. In the x-axis the different paired comparisons are represented. The horizontal line within each box represents the median, the edges of the box represent the first and third quartile, whiskers mark to the most extreme data points that are not considered outliers.

[3] F. Lotte, L. Bougrain, A. Cichocki, M. Clerc, M. Congedo, A. Rakotomamonjy, F. Yger, A review of classification algorithms for EEG-based brain–computer interfaces: a 10 year update, Journal of Neural Engineering 15 (3) (2018) 031005.

[4] J. Deng, J. Yao, J. P. Dewald, Classification of the intention to generate a shoulder versus elbow torque by means of a time–frequency synthesized spatial patterns BCI algorithm, Journal of Neural Engineering 2 (4) (2005) 131.

[5] E. López-Larraz, A. Sarasola-Sanz, N. Irastorza-Landa, N. Birbaumer, A. Ramos-Murguialday, Brain-machine interfaces for rehabilitation in stroke: A review, NeuroRehabilitation 43 (1) (2018) 77–97.

[6] P. Ofner, A. Schwarz, J. Pereira, G. R. Müller-Putz, Upper limb movements can be decoded from the time-domain of low-frequency EEG, PloS one 12 (8) (2017) e0182578.

[7] J. R. Millan, On the need for on-line learning in brain-computer interfaces, in: 2004 IEEE International Joint Conference on Neural Networks (IJCNN), Vol. 4, IEEE, 2004, pp. 2877–2882.

[8] M. Grosse-Wentrup, What are the causes of performance variation in brain-

computer interfacing?, International Journal of Bioelectromagnetism 13 (3) (2011) 115–116.

[9] F. Lotte, C. Jeunet, Online classification accuracy is a poor metric to study mental imagery-based BCI user learning: an experimental demonstration and new metrics, in: 7th International BCI Conference, 2017, pp. hal–01519478.

[10] P. Shenoy, M. Krauledat, B. Blankertz, R. P. Rao, K.-R. Müller, Towards adaptive classification for BCI, Journal of Neural Engineering 3 (1) (2006) R13–23.

[11] P. L. Nunez, R. Srinivasan, Electric fields of the brain, The neurophysics of EEG, New York, Oxford University Press, 2006.

[12] N. Mammone, S. De Salvo, C. Ieracitano, S. Marino, A. Marra, F. Corallo, F. Morabito, A permutation disalignment index-based complex network approach to evaluate longitudinal changes in brain-electrical connectivity, Entropy 19 (10) (2017) 548.

[13] N. Mammone, S. De Salvo, L. Bonanno, C. Ieracitano, S. Marino, A. Marra, A. Bramanti, F. C. Morabito, Brain network analysis of compressive sensed high-density EEG signals in AD and MCI subjects, IEEE Transactions on Industrial Informatics 15 (1) (2018) 527–536.

[14] P. S. Hammon, S. Makeig, H. Poizner, E. Todorov, V. R. De Sa, Predicting reaching targets from human EEG, IEEE Signal Processing Magazine 25 (1) (2007) 69–77.

[15] J. C. Henry, Electroencephalography: basic principles, clinical applications, and related fields, Neurology 67 (11) (2006) 2092–2092.

[16] D. J. McFarland, J. R. Wolpaw, Brain-computer interfaces for communication and control, Communications of the ACM 54 (5) (2011) 60.

[17] B. J. Edelman, B. Baxter, B. He, EEG source imaging enhances the decoding of complex right-hand motor imagery tasks, IEEE Transactions on Biomedical Engineering 63 (1) (2015) 4–14.

[18] A. Shakeel, M. S. Navid, M. N. Anwar, S. Mazhar, M. Jochumsen, I. K. Niazi, A review of techniques for detection of movement intention using movement-related cortical potentials, Computational and mathematical methods in medicine (2015) 346217.

[19] G. Vecchiato, M. Del Vecchio, L. Ascari, S. Antopolskiy, F. Deon, L. Kubin, J. Ambeck-Madsen, G. Rizzolatti, P. Avanzini, Electroencephalographic time-frequency patterns of braking and acceleration movement preparation in car driving simulation, Brain research 1716 (2019) 16–26.

[20] J. Wagner, S. Makeig, M. Gola, C. Neuper, G. Müller-Putz, Distinct β band oscillatory networks subserving motor and cognitive control during gait adaptation, Journal of Neuroscience 36 (7) (2016) 2212–2226.

[21] M. Seeber, R. Scherer, G. R. Müller-Putz, EEG oscillations are modulated in different behavior-related networks during rhythmic finger movements, Journal of Neuroscience 36 (46) (2016) 11671–11681.

[22] X. Yong, C. Menon, EEG classification of different imaginary movements within the same limb, PloS one 10 (4) (2015) e0121896.

[23] N. Lu, T. Li, X. Ren, H. Miao, A deep learning scheme for motor imagery classification based on restricted Boltzmann machines, IEEE transactions on neural systems and rehabilitation engineering 25 (6) (2016) 566–576.

[24] Y. R. Tabar, U. Halici, A novel deep learning approach for classification of EEG motor imagery signals, Journal of Neural Engineering 14 (1) (2016) 016003.

[25] I. Sturm, S. Lapuschkin, W. Samek, K.-R. Müller, Interpretable deep neural networks for single-trial EEG classification, Journal of neuroscience methods 274 (2016) 141–145.

[26] R. T. Schirrmeister, J. T. Springenberg, L. D. J. Fiederer, M. Glasstetter, K. Eggensperger, M. Tangermann, F. Hutter, W. Burgard, T. Ball, Deep learning with convolutional neural networks for EEG decoding and visualization, Human brain mapping 38 (11) (2017) 5391–5420.

[27] K.-W. Ha, J.-W. Jeong, Motor imagery EEG classification using capsule networks, Sensors 19 (13) (2019) 2854.

[28] E. Lew, R. Chavarriaga, S. Silvoni, J. d. R. Millán, Detection of self-paced reaching movement intention from EEG signals, Frontiers in neuroengineering 5 (2012) 13.

[29] L. Yang, H. Leung, M. Plank, J. Snider, H. Poizner, EEG activity during movement planning encodes upcoming peak speed and acceleration and improves the accuracy in predicting hand kinematics, IEEE journal of biomedical and health informatics 19 (1) (2015) 22–28.

[30] H. Kim, N. Yoshimura, Y. Koike, Classification of movement intention using independent components of premovement EEG, Frontiers in human neuroscience 13 (2019) 63.

[31] C. Ieracitano, N. Mammone, A. Bramanti, A. Hussain, F. C. Morabito, A convolutional neural network approach for classification of dementia stages based on 2d-spectral representation of EEG recordings, Neurocomputing 323 (2019) 96–107.

[32] F. C. Morabito, M. Campolo, C. Ieracitano, J. M. Ebadi, L. Bonanno, A. Bramanti, S. Desalvo, N. Mammone, P. Bramanti, Deep convolutional neural networks for classification of Mild Cognitive Impaired and Alzheimer's disease patients from scalp EEG recordings, in: 2016 IEEE 2nd International Forum on Research and Technologies for Society and Industry Leveraging a better tomorrow (RTSI), IEEE, (2016), pp. 1–6.

[33] S. Gasparini, M. Campolo, C. Ieracitano, N. Mammone, E. Ferlazzo, C. Sueri, G. Tripodi, U. Aguglia, F. Morabito, Information theoretic-based interpretation of a deep neural network approach in diagnosing psychogenic non-epileptic seizures, Entropy 20 (2) (2018) 43.

[34] D. Hermes, M. J. Vansteensel, A. M. Albers, M. G. Bleichner, M. R. Benedictus, C. M. Orellana, E. Aarnoutse, N. Ramsey, Functional MRI-based identification of brain areas involved in motor imagery for implantable brain–computer interfaces, Journal of Neural Engineering 8 (2) (2011) 025007.

[35] S. S. Kantak, J. W. Stinear, E. R. Buch, L. G. Cohen, Rewiring the brain: potential role of the premotor cortex in motor control, learning, and recovery of function following brain injury, Neurorehabilitation and neural repair 26 (3) (2012) 282–292.

[36] R. Grech, T. Cassar, J. Muscat, K. P. Camilleri, S. G. Fabri, M. Zervakis, P. Xanthopoulos, V. Sakkalis, B. Vanrumste, Review on solving the inverse problem in EEG source analysis, Journal of neuroengineering and rehabilitation 5 (1) (2008) 25.

[37] S. Haufe, A. Ewald, A simulation framework for benchmarking EEG-based brain connectivity estimation methodologies, Brain topography (2016) 1–18.

[38] S. Haufe, Y. Huang, L. C. Parra, A highly detailed FEM volume conductor model based on the ICBM152 average head template for EEG source imaging and TCS targeting, in: Conf Proc IEEE Eng Med Biol Soc, 2015.

[39] F. Tadel, S. Baillet, J. C. Mosher, D. Pantazis, R. M. Leahy, Brainstorm: a user-friendly application for MEG/EEG analysis, Computational intelligence and neuroscience (2011) 8.

[40] S. Baillet, J. C. Mosher, R. M. Leahy, Electromagnetic brain mapping, IEEE Signal processing magazine 18 (6) (2001) 14–30.

[41] M. Grosse-Wentrup, C. Liefhold, K. Gramann, M. Buss, Beamforming in noninvasive brain-computer interfaces, IEEE Transactions on Biomedical Engineering 56 (4) (2009) 1209–1219.

[42] K. Brodmann, Brodmann's: Localisation in the cerebral cortex, Springer Science & Business Media, (2007).

[43] J. L. Lancaster, D. Tordesillas-Gutiérrez, M. Martinez, F. Salinas, A. Evans, K. Zilles, J. C. Mazziotta, P. T. Fox, Bias between MNI and Talairach coordinates analyzed using the ICBM-152 brain template, Human brain mapping 28 (11) (2007) 1194–1205.

[44] J. L. Lancaster, L. Rainey, J. Summerlin, C. Freitas, P. T. Fox, A. Evans, A. Toga, J. Mazziotta, Automated labeling of the human brain: A preliminary report on the development and evaluation of a forward-transform method, Human brain mapping 5 (4) (1997) 238–242.

[45] J. L. Lancaster, M. G. Woldorff, L. M. Parsons, M. Liotti, C. S. Freitas, L. Rainey, P. V. Kochunov, D. Nickerson, S. A. Mikiten, P. T. Fox, Automated Talairach atlas labels for functional brain mapping, Human brain mapping 10 (3) (2000) 120–131.

[46] Neucube: A spiking neural network architecture for mapping, learning and understanding of spatio-temporal brain data, Neural Networks 52 (2014) 62 – 76.

[47] I. Daubechies, Ten Lectures on Wavelets, Society for Industrial and Applied Mathematics, 1992.

[48] A. Kilicarslan, J. L. Contreras-Vidal, Characterization and real-time removal of motion artifacts from EEG signals, Journal of Neural Engineering 16 (5) (2019) 056027.

[49] J. N. Spring, N. Place, F. Borrani, B. Kayser, J. Barral, Movement-related cortical potential amplitude reduction after cycling exercise relates to the extent of neuromuscular fatigue, Frontiers in human neuroscience 10 (2016) 257.

[50] S. Muthukumaraswamy, High-frequency brain activity and muscle artifacts in MEG/EEG: a review and recommendations, Frontiers in human neuroscience 7 (2013) 138.

[51] A. Krizhevsky, I. Sutskever, G. E. Hinton, Imagenet classification with deep convolutional neural networks, in: Advances in neural information processing systems, 2012, pp. 1097–1105.

[52] V. Nair, G. E. Hinton, Rectified linear units improve restricted boltzmann machines, in: Proceedings of the 27th international conference on machine learning (ICML-10), 2010, pp. 807–814.

[53] D. P. Kingma, J. Ba, Adam: A method for stochastic optimization, arXiv preprint arXiv:1412.6980.

[54] Y. Bengio, Practical recommendations for gradient-based training of deep architectures, in: Neural networks: Tricks of the trade (2012) 437–478.

[55] D. M. Powers, Evaluation: from precision, recall and f-measure to roc, informedness, markedness and correlation, Journal of Machine Learning Technologies 2(1) (2011) 37–63.

[56] J. Song, C. Davey, C. Poulsen, P. Luu, S. Turovets, E. Anderson, K. Li, D. Tucker, EEG source localization: sensor density and head surface coverage, Journal of neuroscience methods 256 (2015) 9–21.

[57] Z. Tang, H. Yu, C. Lu, P. Liu, X. Jin, Single-trial classification of different movements on one arm based on ERD/ERS and corticomuscular coherence, IEEE Access 7 (2019) 128185–128197.

[58] Z.-c. Tang, C. Li, J.-f. Wu, P.-c. Liu, S.-w. Cheng, Classification of eeg-based single-trial motor imagery tasks using a b-csp method for bci, Frontiers of Information Technology & Electronic Engineering 20 (8) (2019) 1087–1098.

[59] A. T. Vourvopoulos, O. M. Pardo, S. Lefebvre, M. Neureither, D. Saldana, E. Jahng, S.-L. Liew, Effects of a brain-computer interface with virtual reality (vr) neurofeedback: A pilot study in chronic stroke patients, Frontiers in Human Neuroscience 13 (2019) 210.

[60] J. Zhang, B. Wang, C. Zhang, Y. Xiao, M. Y. Wang, An EEG/EMG/EOG-based multimodal human-machine interface to real-time control of a soft robot hand, Frontiers in neurorobotics 13 (2019) 7.

[61] Z. Tayeb, N. Waniek, J. Fedjaev, N. Ghaboosi, L. Rychly, C. Widderich, C. Richter, J. Braun, M. Saveriano, G. Cheng, et al., Gumpy: A python toolbox suitable for hybrid brain–computer interfaces, Journal of Neural Engineering 15 (6) (2018) 065003.

[62] S. Balasubramanian, E. Garcia-Cossio, N. Birbaumer, E. Burdet, A. Ramos-Murguialday, Is emg a viable alternative to BCI for detecting movement intention in severe stroke?, IEEE Transactions on Biomedical Engineering 65 (12) (2018) 2790–2797.

Table 2: Accuracies (ACC) of the premov vs. premov and premov vs. rest classification type estimated on the test sets. All the results are expressed as avg(value) ± std(value).

Classification type	Classification task	S01	S02	S03	S04	S05	S06	S07	S08	S09	S10	S11	S12	S13	S14	S15	Average
premov vs. premov	HC vs. HO	54.37±0.083	63.10±0.042	92.46±0.047	92.06±0.041	55.16±0.094	60.32±0.059	50.00±0.045	63.10±0.059	57.94±0.071	59.13±0.064	54.37±0.093	56.35±0.080	55.16±0.071	68.65±0.057	64.01±0.071	**63.07±0.064**
	HC vs. PR	61.39±0.049	56.35±0.066	92.06±0.047	89.58±0.043	55.56±0.039	67.86±0.031	52.78±0.077	61.51±0.081	59.92±0.066	79.37±0.048	55.16±0.054	55.95±0.071	72.22±0.058	76.19±0.048	69.85±0.023	**67.05±0.055**
	HC vs. EE	57.54±0.101	65.87±0.038	89.29±0.052	92.46±0.045	58.73±0.101	56.35±0.071	58.33±0.085	58.33±0.064	64.68±0.075	86.11±0.042	62.70±0.077	64.29±0.078	68.25±0.060	76.98±0.069	71.40±0.061	**68.75±0.068**
	HC vs. EF	59.13±0.059	61.11±0.075	86.51±0.054	94.44±0.039	64.29±0.044	59.92±0.092	66.27±0.054	69.44±0.062	62.70±0.083	77.78±0.039	61.11±0.073	50.79±0.047	72.62±0.079	70.63±0.068	70.11±0.055	**69.12±0.062**
	HC vs. SU	59.13±0.096	52.38±0.049	86.11±0.051	91.27±0.054	65.48±0.080	77.38±0.074	59.52±0.077	61.51±0.047	64.29±0.061	73.41±0.045	67.86±0.048	64.29±0.061	72.62±0.072	72.62±0.061	69.88±0.085	**69.18±0.062**
	HO vs. PR	49.03±0.043	54.37±0.053	61.11±0.060	76.83±0.060	53.97±0.071	59.92±0.064	53.57±0.078	65.08±0.055	65.48±0.096	67.46±0.098	53.97±0.106	51.98±0.059	69.84±0.025	65.08±0.064	61.75±0.076	**60.62±0.066**
	HO vs. EE	46.83±0.063	64.68±0.066	80.16±0.044	97.62±0.025	59.13±0.055	61.51±0.081	56.75±0.042	63.49±0.084	59.52±0.104	75.40±0.057	63.89±0.070	57.94±0.052	69.44±0.064	71.83±0.067	69.45±0.052	**66.50±0.062**
	HO vs. EF	58.73±0.082	64.29±0.057	70.63±0.062	98.41±0.027	55.95±0.087	61.11±0.073	56.35±0.086	69.84±0.061	56.75±0.101	62.30±0.078	58.73±0.071	53.97±0.071	70.24±0.092	71.43±0.059	66.74±0.081	**65.03±0.071**
	HO vs. SU	42.46±0.073	50.40±0.057	76.98±0.086	92.86±0.042	61.51±0.057	71.03±0.058	56.35±0.092	67.46±0.066	50.79±0.075	64.68±0.098	58.33±0.075	56.75±0.045	65.08±0.083	65.48±0.078	64.11±0.035	**62.95±0.070**
	PR vs. EE	50.19±0.034	53.57±0.052	65.87±0.076	94.21±0.045	62.30±0.058	57.94±0.086	55.95±0.090	59.13±0.107	68.65±0.084	69.84±0.076	55.16±0.054	60.32±0.038	67.46±0.096	63.89±0.075	55.95±0.082	**62.70±0.070**
	PR vs. EF	61.78±0.074	51.59±0.091	65.48±0.119	93.05±0.041	58.73±0.063	50.79±0.110	54.76±0.067	63.10±0.075	59.52±0.053	66.67±0.072	53.97±0.039	45.24±0.067	69.44±0.103	54.76±0.084	47.10±0.051	**59.73±0.074**
	PR vs. SU	43.63±0.079	51.19±0.031	51.98±0.081	85.33±0.070	49.60±0.074	52.38±0.101	48.02±0.094	53.97±0.045	49.21±0.098	51.59±0.086	51.59±0.068	50.40±0.079	49.21±0.055	55.95±0.052	52.38±0.061	**53.09±0.072**
	EE vs. EF	54.76±0.067	49.60±0.057	55.95±0.052	53.17±0.061	56.35±0.086	53.17±0.037	56.35±0.059	54.37±0.110	59.13±0.071	59.92±0.078	46.43±0.104	48.41±0.058	51.19±0.109	50.79±0.112	49.80±0.043	**53.29±0.074**
	EE vs. SU	42.86±0.070	57.14±0.045	55.56±0.120	57.14±0.092	59.92±0.086	57.14±0.082	54.37±0.104	53.97±0.035	54.37±0.105	59.13±0.084	64.68±0.097	69.44±0.051	60.71±0.065	69.44±0.085	63.45±0.085	**58.62±0.080**
	EF vs. SU	46.43±0.035	61.11±0.098	55.95±0.072	57.94±0.086	55.56±0.048	61.51±0.065	52.78±0.083	64.29±0.044	54.76±0.057	57.54±0.076	63.10±0.071	63.10±0.090	53.17±0.090	55.56±0.053	57.55±0.083	**57.36±0.070**
	Average	**52.55±0.067**	**57.12±0.058**	**72.41±0.068**	**84.43±0.051**	**58.15±0.070**	**60.56±0.072**	**55.48±0.076**	**61.90±0.066**	**59.18±0.080**	**67.35±0.070**	**58.07±0.073**	**56.61±0.063**	**64.44±0.075**	**65.95±0.069**	**62.23±0.060**	**62.47±0.067**
premov vs. rest	HC vs. RE	92.86±0.048	95.24±0.045	95.24±0.038	96.43±0.014	79.37±0.089	77.78±0.042	76.98±0.124	83.33±0.106	98.41±0.015	97.62±0.034	83.73±0.057	84.52±0.071	92.46±0.081	90.08±0.062	89.99±0.031	**88.93±0.059**
	HO vs. RE	86.90±0.073	93.25±0.031	97.22±0.032	97.22±0.039	90.08±0.027	83.33±0.064	78.17±0.069	92.86±0.060	96.03±0.035	96.83±0.034	88.10±0.055	85.71±0.034	92.06±0.034	90.48±0.048	91.44±0.056	**90.64±0.045**
	PR vs. RE	91.51±0.036	95.24±0.031	93.25±0.058	90.35±0.041	92.06±0.037	82.14±0.045	74.60±0.103	89.68±0.067	96.03±0.050	97.22±0.032	87.30±0.133	88.89±0.058	91.27±0.052	92.46±0.055	92.46±0.055	**91.33±0.057**
	EE vs. RE	92.06±0.061	92.46±0.042	94.44±0.048	88.89±0.060	81.35±0.078	80.95±0.065	74.70±0.093	86.11±0.075	97.22±0.028	100.00±0.000	88.10±0.064	85.71±0.044	89.29±0.072	94.84±0.025	80.95±0.082	**88.47±0.056**
	EF vs. RE	95.24±0.038	94.84±0.034	90.87±0.078	82.54±0.064	90.87±0.055	80.16±0.059	75.00±0.103	84.52±0.042	94.44±0.042	97.62±0.030	82.14±0.095	82.14±0.091	87.30±0.055	90.48±0.088	75.68±0.136	**86.92±0.067**
	SU vs. RE	92.46±0.042	93.25±0.045	93.25±0.086	84.92±0.068	88.89±0.075	85.32±0.031	81.75±0.095	86.90±0.031	93.65±0.042	95.63±0.022	87.70±0.039	89.68±0.042	92.06±0.044	92.06±0.054	81.75±0.106	**89.29±0.055**
	Average	**91.84±0.050**	**94.05±0.038**	**94.05±0.057**	**90.06±0.048**	**87.10±0.060**	**81.61±0.051**	**76.85±0.098**	**87.24±0.064**	**95.97±0.035**	**97.49±0.025**	**86.18±0.074**	**86.11±0.056**	**90.74±0.056**	**91.73±0.055**	**85.37±0.066**	**90.30±0.056**

Table 3: F-score of the premov vs. premov and premov vs. rest classification type estimated on the test sets. All the results are expressed as avg(value) ± std(value).

Classification type	Classification task	S01	S02	S03	S04	S05	S06	S07	S08	S09	S10	S11	S12	S13	S14	S15	Average
premov vs. premov	HC vs. HO	54.12±0.091	64.50±0.073	91.85±0.058	92.15±0.040	49.56±0.129	51.33±0.156	48.56±0.077	62.21±0.065	58.48±0.083	61.83±0.042	54.67±0.106	54.43±0.128	55.44±0.082	71.42±0.059	63.25±0.088	**62.25±0.085**
	HC vs. PR	64.35±0.051	54.44±0.057	92.02±0.049	90.02±0.039	56.27±0.059	68.15±0.055	51.78±0.069	55.83±0.157	60.04±0.094	78.03±0.055	57.64±0.064	53.77±0.074	70.98±0.075	77.30±0.038	67.50±0.061	**66.54±0.066**
	HC vs. EE	54.86±0.167	61.96±0.053	89.22±0.054	92.77±0.041	60.04±0.102	57.69±0.130	56.14±0.094	60.92±0.058	58.22±0.112	86.75±0.038	60.23±0.089	60.07±0.118	67.41±0.076	75.35±0.081	70.15±0.067	**67.45±0.085**
	HC vs. EF	59.93±0.061	58.82±0.061	86.35±0.059	94.85±0.035	64.47±0.046	58.55±0.152	65.88±0.048	69.18±0.070	60.57±0.105	77.87±0.044	58.99±0.117	57.52±0.077	72.28±0.077	70.05±0.071	69.23±0.063	**68.30±0.072**
	HC vs. SU	60.48±0.090	48.76±0.094	85.67±0.053	91.05±0.057	64.27±0.080	74.32±0.098	61.50±0.078	59.75±0.080	66.52±0.042	73.32±0.040	67.93±0.087	58.80±0.123	73.98±0.069	71.57±0.063	70.42±0.066	**68.42±0.075**
	HO vs. PR	49.77±0.051	51.87±0.098	58.83±0.078	78.19±0.050	54.03±0.054	60.28±0.061	55.92±0.099	62.47±0.098	65.70±0.110	65.80±0.111	55.64±0.164	47.11±0.109	69.06±0.045	64.47±0.095	60.80±0.077	**59.99±0.087**
	HO vs. EE	45.68±0.142	62.14±0.085	79.33±0.044	97.66±0.024	59.02±0.059	56.97±0.118	56.69±0.066	62.89±0.093	57.10±0.114	77.79±0.053	65.03±0.068	56.21±0.101	69.95±0.072	72.79±0.078	67.79±0.078	**65.80±0.079**
	HO vs. EF	57.50±0.104	63.25±0.079	67.74±0.091	98.50±0.026	50.44±0.156	59.26±0.121	55.80±0.127	69.92±0.068	52.65±0.134	66.16±0.069	58.06±0.063	56.68±0.054	70.37±0.089	69.86±0.067	68.91±0.061	**61.45±0.087**
	HO vs. SU	44.03±0.043	57.11±0.065	77.73±0.089	92.61±0.043	61.97±0.126	70.01±0.063	61.08±0.064	66.72±0.050	50.07±0.108	61.70±0.109	55.62±0.123	53.52±0.075	65.16±0.100	65.19±0.091	65.15±0.100	**64.54±0.083**
	PR vs. EE	49.09±0.087	54.43±0.109	65.77±0.060	94.55±0.043	62.84±0.077	57.18±0.105	56.39±0.091	59.54±0.118	70.48±0.075	70.21±0.071	51.59±0.095	59.20±0.085	68.44±0.066	63.69±0.086	50.89±0.172	**62.29±0.089**
	PR vs. EF	60.44±0.108	54.45±0.078	65.09±0.134	93.55±0.039	60.08±0.082	45.58±0.180	57.10±0.075	63.14±0.092	59.27±0.093	66.74±0.077	53.41±0.111	45.83±0.159	69.69±0.108	52.20±0.094	46.11±0.101	**59.51±0.102**
	PR vs. SU	41.44±0.076	48.98±0.202	50.47±0.096	83.56±0.081	52.07±0.075	52.52±0.107	50.33±0.098	54.77±0.059	46.38±0.118	50.73±0.134	43.08±0.130	46.18±0.143	50.35±0.076	51.56±0.097	54.81±0.102	**51.82±0.106**
	EE vs. EF	54.08±0.092	46.34±0.090	55.69±0.090	50.93±0.080	53.84±0.102	53.12±0.062	51.87±0.139	50.15±0.117	60.20±0.087	59.47±0.145	43.43±0.141	46.05±0.105	47.37±0.080	49.16±0.149	47.22±0.038	**51.26±0.101**
	EE vs. SU	41.92±0.170	59.72±0.088	55.12±0.156	57.60±0.110	61.94±0.091	54.08±0.097	56.52±0.098	52.88±0.089	53.31±0.147	59.73±0.090	64.80±0.108	66.42±0.079	60.50±0.061	68.86±0.074	64.98±0.060	**58.56±0.101**
	EF vs. SU	45.91±0.102	66.00±0.081	54.81±0.097	61.58±0.081	54.53±0.053	61.34±0.078	58.73±0.074	67.78±0.054	52.83±0.081	56.63±0.091	63.16±0.070	57.71±0.157	55.41±0.103	52.98±0.075	56.11±0.129	**57.70±0.088**
	Average	**52.24±0.096**	**56.85±0.087**	**71.71±0.081**	**84.64±0.053**	**57.69±0.086**	**58.69±0.106**	**56.28±0.086**	**61.21±0.084**	**58.12±0.100**	**67.52±0.078**	**56.89±0.102**	**54.63±0.106**	**64.43±0.079**	**65.10±0.081**	**60.92±0.085**	**64.97±0.087**
premov vs. rest	HC vs. RE	92.86±0.047	95.33±0.041	95.01±0.042	96.30±0.015	77.39±0.123	80.22±0.033	79.04±0.100	82.52±0.103	98.43±0.015	97.76±0.031	81.72±0.070	85.27±0.055	92.60±0.081	90.71±0.051	89.99±0.051	**89.01±0.057**
	HO vs. RE	86.14±0.081	93.49±0.029	97.04±0.035	97.27±0.037	89.91±0.025	85.68±0.045	76.35±0.086	92.60±0.061	95.94±0.038	96.95±0.032	87.88±0.053	85.05±0.029	92.27±0.033	90.05±0.056	91.12±0.035	**90.47±0.043**
	PR vs. RE	91.47±0.038	95.35±0.027	92.93±0.062	90.48±0.037	92.00±0.036	84.19±0.030	68.74±0.143	89.50±0.065	96.10±0.047	97.34±0.030	82.32±0.241	87.83±0.073	90.51±0.059	92.46±0.053	92.46±0.053	**89.57±0.067**
	EE vs. RE	91.91±0.062	92.92±0.036	94.32±0.047	89.21±0.053	82.73±0.062	83.80±0.044	69.10±0.191	83.80±0.113	97.11±0.030	100.00±0.000	87.80±0.066	84.48±0.053	88.95±0.067	94.75±0.026	82.10±0.084	**88.20±0.062**
	EF vs. RE	94.99±0.042	94.91±0.032	90.70±0.088	81.39±0.100	90.88±0.055	82.50±0.046	69.51±0.218	84.38±0.035	94.30±0.045	97.72±0.028	81.74±0.090	83.54±0.082	86.46±0.067	91.63±0.072	73.29±0.206	**86.53±0.080**
	SU vs. RE	92.90±0.039	93.28±0.046	94.07±0.069	83.84±0.082	88.47±0.078	83.96±0.041	78.76±0.155	86.83±0.051	93.46±0.046	95.71±0.021	88.54±0.038	89.90±0.047	92.53±0.037	92.82±0.045	79.31±0.137	**88.96±0.062**
	Average	**91.71±0.051**	**94.21±0.035**	**94.01±0.057**	**89.75±0.054**	**86.90±0.063**	**83.39±0.040**	**73.58±0.149**	**86.60±0.071**	**95.89±0.037**	**97.58±0.024**	**85.00±0.093**	**86.01±0.056**	**90.55±0.057**	**92.07±0.051**	**89.99±0.072**	**88.79±0.061**